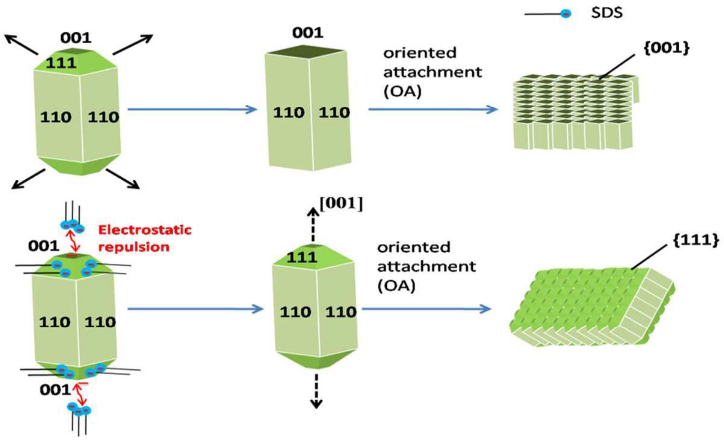
SDS
001
111
110 110
001
110 110
oriented attachment (OA)
{001}
[001]
Electrostatic repulsion
001
110 110
001
111
110 110
oriented attachment (OA)
{111}

SDS-assisted solvothermal synthesis of rose-like BiOBr partially enclosed by {111} facets and enhanced visible-light photocatalytic activity

Yang Zhao[a§], Tao Yu[a,c,d*§], Xin Tan[b], Chuang Xie[a,d], Shucong Wang[e]

[a]*School of Chemical Engineering and Technology, Tianjin University, Tianjin 300072, P.R. China*
[b]*School of Science, Tibet University, Lhasa 850000, P.R. China*
[c]*Tianjin University-National Institute for Materials Science Joint Research Center, Tianjin University, Tianjin 300072, P.R. China*
[d]*Collaborative Innovation Center of Chemical Science and Engineering (Tianjin), Tianjin 300072, P.R. China*
[e]*School of Environmental Science and Engineering, Tianjin University, Tianjin 300072, P.R. China*

§Yang Zhao and Tao Yu contributed equally to this work.

*Corresponding author. Tel.:/Fax +86 2223502142.

E-mail addresses: yutao@tju.edu.cn, lisat0001@163.com (T.Yu).

Abstract Rose-like BiOBr nanostructures with exposed {111} facets were firstly synthesized with the assistance of anionic surfactant sodium dodecyl sulfate (SDS) via a facile solvothermal route. The 2D nanosheets, which self-assembled to form the 3D structures, were achieved with the thickness decreasing from average 120 nm to 20 nm. Specially, the nanosheets were partially enclosed by {111} facets due to the effect of SDS. The as-prepared BiOBr with {111} facets exhibited excellent electrochemical behavior and photocatalytic activity under both visible light ($\lambda \geq 420$ nm) and monochromatic light ($\lambda = 420$ nm) irradiation.

Keywords Bismuth oxybromide; Photocatalytic activity; SDS; Facet-dependent; Visible light; Solvothermal

1. Introduction

Nowadays, there is an enormous interest in tailoring the morphology and exposed crystal facets of semiconductor materials, because the change of shapes and surface properties can lead to an improvement in photocatalytic and photoelectric properties. For example, Lu and co-workers [1] demonstrated for the first time that TiO_2 single crystals with high percentage of exposed {001} facets could be obtained by using F^- as a capping agent. Then in the past ten years, intense theoretical and experimental studies focused on the fabrication of different facets in TiO_2 [2-7] as well as other semiconductors, such as $BiOV_4$ [8-9], Ag_3PO_4 [10-13], Cu_2O [14], etc. Although the high-energy facets exhibit higher activity than low-energy facets, they easily eliminate because the fastest crystal growth would occur in the direction perpendicular to the high-energy facet. Organic molecules, inorganic ions or their mixtures as capping agents have been applied to the control of growth rate in a certain orientation [15].

Bismuth oxyhalides BiOX (X=Cl, Br, I), as alternative photocatalysts, have layered tetragonal matlockite structure with $[Bi_2O_2]$ slabs interleaved by double slabs of halogen atoms along the [001] direction. The internal static electric fields between the $[Bi_2O_2]^{2+}$ and halogen anionic layers are believed to improve the separation of photo-generated electron-hole pairs [16]. Recently, many efforts were paid for further enhancing the photocatalytic activity of BiOX, such as tailoring morphology [17-21], metal (or semiconductor) coupling[22-25], and facet-controlled fabrication[26-32], etc., To date, reports focused on crystal-facet-controlled fabrication of BiOX are limited to {001}[26-31], {010}[27]and {102}[32] facets. To the best of our knowledge, {111} facets of BiOX have not been investigated. Moreover, it is still rare in the literature about the preparation of BiOX with the assistance of anionic surfactant sodium dodecyl sulfate (SDS).

Herein, we first report on the facet-controllable synthesis of BiOBr 3D micro-flower which is composed of 2D nanosheets partially enclosed by {111} facets by using sodium dodecyl sulfate (SDS) as capping agent. Furthermore, studies of photocatalytic and electrochemical performances reveal that the BiOBr with {111} facet exhibits higher activity than BiOBr with {001} facet prepared in the absence of SDS.

2. Experimental

2.1 Preparation of BiOBr photocatalysts

BiOBr micro-flowers enclosed by {111} facets (noted as BiOBr-111) were prepared by a simple solvothermal method. All raw materials were commercially available and used without any treatment. Typically, 1 mmol of KBr and 0.2 g of SDS were dissolved in 20 mL ethylene glycol (EG). Then the above solution was slowly added into the same amount of EG solution containing stoichiometric amount of $Bi(NO_3)_3 \cdot 5H_2O$. The mixture was stirred for 30 min at room temperature before poured into a Teflon-lined stainless steel autoclave (50 mL volume). The autoclave was maintained at 120 ℃ for 8 h and then cooled to room temperature. The resulting precipitate was washed successively with deionized water and ethanol six times by centrifugation, and finally dried before characterization. The contrast sample in the absence of SDS (noted as BiOBr-001) was prepared following the same procedure.

2.2 Characterization

The crystal structure of the samples was identified by X-ray diffraction (XRD, Rigaku D/MAX-2500) with Cu Kα radiation. X-ray photoelectron spectroscopy (XPS) was employed for the measurement of composition and chemical states of the samples. The morphology of BiOBr was observed using field emission scanning electron microscope (FESEM, FEI Nanosem 430). The high-resolution transmission electron microscopy (HRTEM) images were taken on a Tecnai G2 F20 transmission electron microscope with an accelerating voltage of 200 kV. The specific surface areas of BiOBr samples were measured and calculated using a Quantachrome Autosorb iQ instrument. The UV-vis diffuse reflectance spectra were measured on a Shimadzu UV-2550 spectrophotometer using $BaSO_4$ as a reference in the wavelength of 200－800 nm.

2.3 Evaluation of photocatalytic performance

The photodegradation of RhB and MO under visible light irradiation was conducted to evaluate the photocatalytic properties of different BiOBr samples. A 300 W Xe lamp (HXS-F/UV 300, Beijing NBet Technology Co., Ltd) was used as light source, and equipped with an ultraviolet cutoff filter ($\lambda \geq 420$ nm) or a band pass filter($\lambda = 420$ nm) to provide different visible light. In each experiment, 50 mg of BiOBr powder was dispersed in 50 mL of 10 mg L^{-1} RhB or MO solution. After that, the suspensions were kept in darkness for 0.5 h with constant stirring before irradiation. During the photodegradation, the light intensity was maintained at about 20 mW cm^{-2}. The concentration variation of RhB or MO was monitored by a UV-vis spectrophotometer (T6, Beijing Purkinje General Instrument Co., Ltd).

In addition, the photocatalytic activities of the BiOBr samples were investigated for the degradation of gaseous acetone under visible light irradiation ($\lambda \geq 420$ nm). 0.1 g of sample powder was uniformly placed on the bottom of a quartz reactor (250 mL in volume). After that, the reactor was sealed and 2 mL of acetone gas was injected into it. Prior to the irradiation, the reactor was kept in darkness for 40 min. The acetone concentration was evaluated using gas chromatography (GC-2014, Shimadzu, Tokyo) every 5 min.

2.4 Photoelectrochemical measurements

Photoelectrochemical properties of BiOBr-001 and BiOBr-111, including the photocurrent and electrochemical impedance spectrum, were evaluated by a standard three-electrode configuration using an electrochemical workstation (CHI660E, Shanghai Chenhua, China) with 1 mol L^{-1} Na_2SO_4 solution as the supporting electrolyte. The prepared photoelectrode (effective area = 1 cm^2), a saturated calomel electrode(SCE) and platinum wire counter electrode (Φ 0.5 mm × 37 mm) acted as the working, reference, and counter electrodes, respectively.

3. Results and discussion

3.1 Morphology and microstructure

The morphology of the products was detected by FESEM. The low-magnification SEM image (Fig. 1a inset) shows that the as-obtained BiOBr-111 products consist of numerous rose-like microstructures with a good polydispersity and narrow size distribution. The average size of the microstructures is about 3μm. The magnified image, as shown in Fig. 1a, reveals that the rose-like microstructure is composed of dozens of radially grown 2D nanosheets with a thickness of about 20 nm and a width of 0.5—1 μm. From Fig. 1b, it can be observed that BiOBr-001 displays a different morphology, although the addition of SDS doesn't change the 3D architecture and size distribution. A careful observation reveals that the microstructure exhibits a square-like hierarchical architecture built from two sides by many 2D nanoplates with a thickness of 100—150 nm. Compared with BiOBr-111, the nanoplates are packed more densely.

The HRTEM images (Fig. 1c and Fig. 1d) exhibit clear lattice fringes, confirming the high crystallinity of both the BiOBr samples. Further observation from the inset of Fig. 1c shows that the lattice spacings of the selected area in BiOBr-111 are 0.278 nm and 0.354 nm, and the angle labeled in the corresponding fast-Fourier transform (FFT) pattern is 50.3°, which is identical to the theoretical value of the {110} and {101} facets. The above structure information indicates that the nanosheets of as-synthesized BiOBr-111 are partially enclosed by {111} facets. The atomic structure of the {111} facets (Fig. 1(e and f)) exhibits open channel feature. However, BiOBr-001 presents a square lattice with the spacing of 0.278 nm, as shown in Fig. 1d, which corresponds to the {110} facets. Based on the FFT pattern (Fig. 1d inset), the spots are assigned to the (110) and (200) planes of BiOBr with the irradiation of electron beam from the [001] direction, confirming that the top and bottom surfaces of the BiOBr nanoplates are identified as {001} facets, while the four lateral surfaces are {110} facets. The {001} facets (Fig. 1g) contain oxygen atoms with high density. The {111} facets also contain terminated oxygen, but the density of oxygen atoms is lower than that of {001} facets.

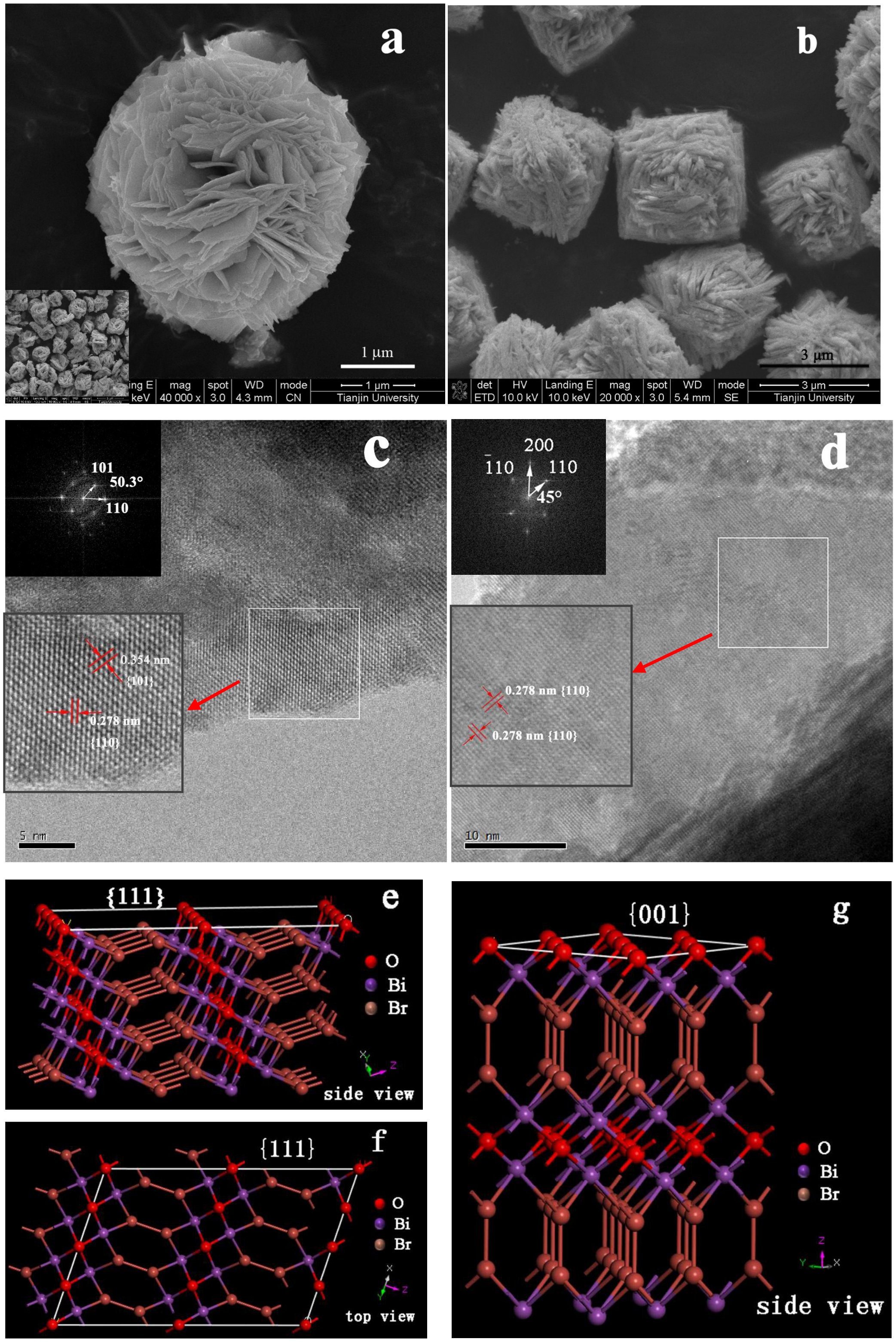

Fig. 1 (a and b) SEM images of BiOBr-111 and BiOBr-001; (c and d) TEM images of BiOBr-111 and BiOBr-001; (e and f) atomic structure of {111} facets; (g) atomic structure of {001} facets.

3.2 Plausible formation mechanisms of the BiOBr hierarchical structure and {111} facets

A set of time-dependent experiments was performed to investigate the plausible formation mechanism of the BiOBr hierarchical structure. In the first two hours of solvothermal, no product can be obtained. After 2 h reaction, the product was composed of a large portion of irregular nanosheets which began to self-assemble to form flower-like structure (Fig. S1(a)). The well-defined 3D flower-like BiOBr formed after 4 h reaction, but the size of the as-prepared BiOBr presented nonuniformity (Fig. S1(b)). When the reaction time lasted for 8 h, large numbers of uniform BiOBr micro-flowers formed. As the reaction time was extended to 24 h, the petals of the BiOBr micro-flowers packed more densely than those obtained at 8 h, and some flowers even began to dehisce(Fig. S1(c)).

From the above results, it can be inferred that the formation of BiOBr 3D hierarchical structure was the combination of four steps: the nucleation of primary particles, crystal growth, oriented attachment and self-assembly, as summarized in Scheme 1. In the initial stage, EG could coordinate with Bi^{3+} to form alkoxide $Bi(OCH_2CH_2OH)^{2+}$ which decreased the concentration of Bi^{3+} in solution, so that the formation of BiOBr nuclei needed a certain temperature and time (Step 1). Then the tiny BiOBr nuclei grew up through the process known as Ostwald ripening (Step 2). Subsequently, the BiOBr nanocrystals rotated adequately to minimize the surface energy and formed nanosheets due to the inner laminar structure of BiOX(Step 3), which is called as oriented attachment. With the increase of reaction time, these individual nanosheets assembled to form 3D microstructures further for the minimization of surface energy (Step 4).

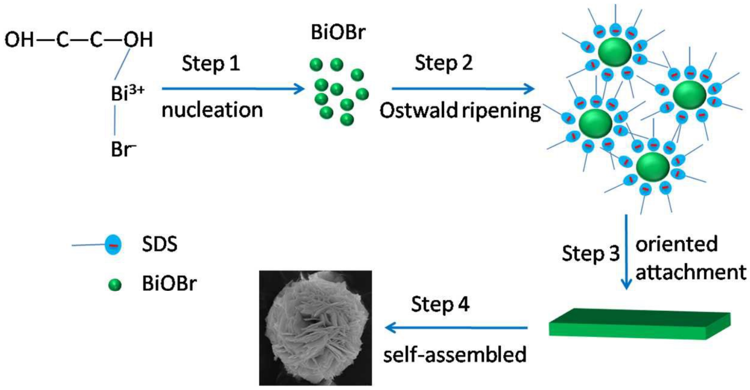

Scheme 1 Plausible formation mechanism of rose-like BiOBr microstructures

It is reasonable to think that SDS plays a key role in the formation of 3D rose-like microstructures and the exposure of {111} facets. SDS is an anionic surfactant containing a sulfate hydrophilic segment, i.e., a sulfonic group, and a hydrocarbon hydrophobic segment. When SDS was involved in the reaction solution, Bi^{3+} of BiOBr nuclei and the sulfonic group of SDS could form ion-pairs due to the electrostatic interaction, so that BiOBr nuclei would be covered by SDS molecules. Then the other side of SDS, the long alkane group, would provide steric repulsion to prevent aggregation. This is the probable reason why the 2D lamellae of BiOBr prepared with SDS are thinner than those without SDS. In addition, since BiOBr has a tetragonal PbFCl-type structure with O-terminated (001) surface as one of the mainly exposed facets[16, 33], the sulfonic group of SDS preferentially adsorbed on other facets which have suitable density of undercoordinated Bi atoms and/or suitable distance between two adjacent undercoordinated Bi atoms on the surfaces[15]. Based on the above analysis, we inferred that the selective adsorption of SDS occurred at {111} facet. This preferential adsorption lowered the surface energy of {111} facet so that the growth rate along [111] orientation could be controlled, which resulted in the exposure of {111} on the surface of nanosheets (as depicted in Scheme 2). Further work is still needed to investigate the exact growth mechanism of {111} facets.

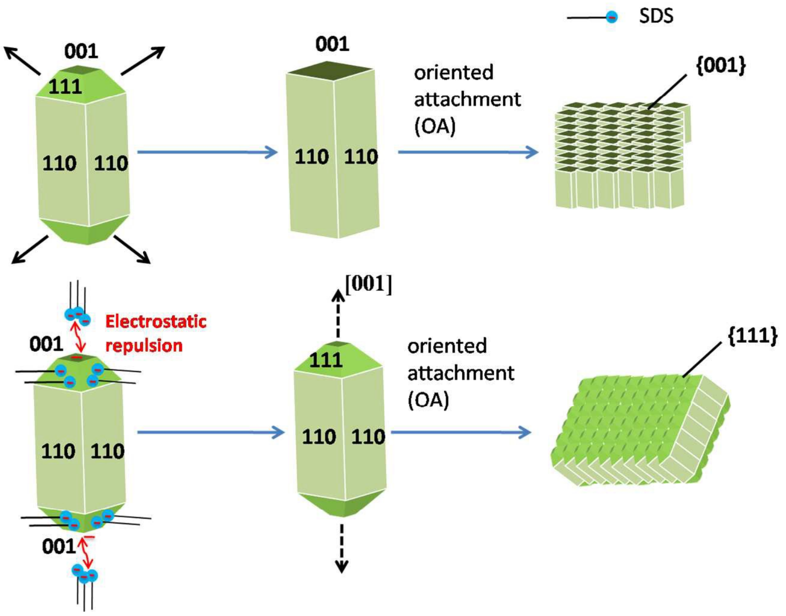

Scheme 2 Plausible formation mechanism of {111} facets

3.3 Phase structure

Fig. 2 shows the XRD patterns of BiOBr-111 and BiOBr-001. All the peaks in black and red curves can be clearly indexed to the tetragonal phase of BiOBr (JCPDS Card No. 09-0393), indicating that the addition of SDS has no effect on the formation of BiOBr crystals. In addition, the diffraction peaks are sharp and intense, suggesting that both the samples were well crystallized. Significantly, the (110)/(102) intensity ratio of BiOBr-111 is 1.04, larger than that of BiOBr-001 (0.94) and JCPDS data(0.65), probably because the BiOBr product with the assistance of SDS had preferred orientation during the synthesis process.

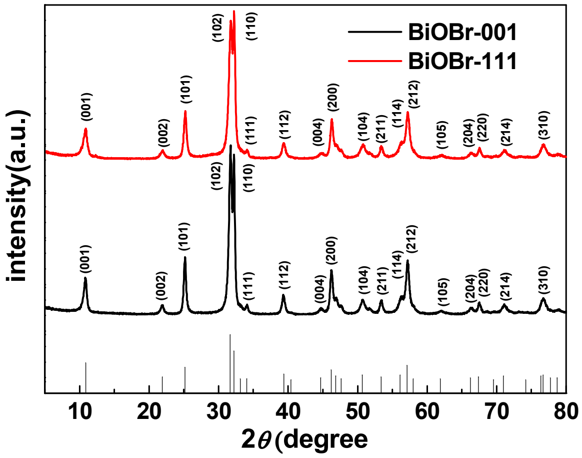

Fig. 2 XRD patterns of the as-prepared BiOBr samples

3.4 Surface composition

The composition and chemical states of BiOBr-111 were investigated by XPS analysis. It can be seen from Fig. 3a that only Bi, O, Br and a trace amount of C are detected, confirming the composition of the sample. The peaks at the binding energy of 159.1 eV and 164.3 eV (Fig. 2b) are assigned to Bi $4f_{7/2}$ and Bi $4f_{5/2}$, respectively, which is the characteristic of Bi^{3+}. The peak located at 68.3 eV (Fig. 2c) is ascribed to Br 3d, corresponding to Br^{-1}. The O 1s signal in Fig. 2d can be fitted by three peaks at 529.94 eV, 531.48 eV and 532.94 eV, since attempts to resolve the signal into only two peaks resulted in an unreasonably large full-width half-maximum (FWHM > 2 eV). The peak at 531.48 eV can be attributed to the O-atoms in the vicinity of an O-vacancy[34], and the others located at 529.94 eV and 532.94 eV are ascribed to lattice oxygen atoms in BiOBr crystal and surface hydroxyl(or crystal water), respectively. The results of XRD and XPS confirm that pure BiOBr can be obtained in the presence of SDS.

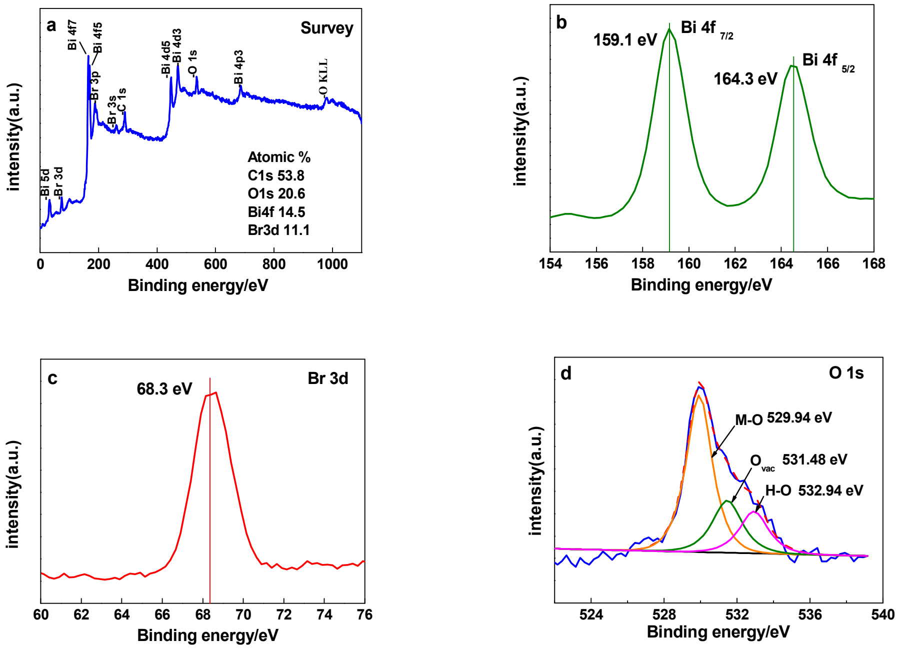

Fig. 3 XPS spectra of BiOBr prepared in the presence of SDS (a) survey scan, (b) Bi 4f, (c) Br 3d and (d) O 1s

3.5 Nitrogen adsorption analysis

The Brunauer-Emmett-Teller (BET) specific surface areas and porosity of the BiOBr samples were investigated by nitrogen adsorption and desorption measurements. The isotherms in Fig. 4 can be categorized as type IV with H3 hysteresis loop observed in the range of 0.4–1.0 p/p_0, which indicates the presence of mesopores. The hysteresis loop in the relative pressure between 0.4 and 0.9 is probably related to the intra-aggregated pores of the BiOBr crystals, which are formed between primary crystallites; while the high-pressure hysteresis loop ($0.9 < p/p_0 < 1$) is probably associated with the textural pores formed between secondary particles due to the aggregation of nanosheets into hierarchical architectures. The BET specific surface area of BiOBr-111 was calculated to be $63.685 m^2/g$, much larger than that of BiOBr-001 ($30.656 m^2/g$). Obviously, high specific surface area of BiOBr-111 means that it has a relatively high surface-to-volume ratio, which is beneficial to enhance the adsorption efficiency of adsorbate molecules.

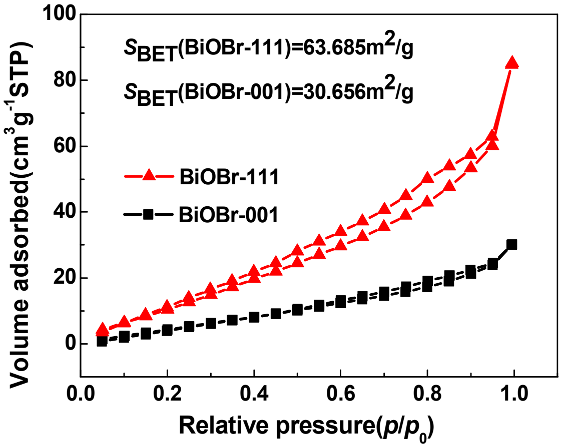

Fig. 4 Nitrogen adsorption/desorption isotherms of the BiOBr samples

3.6 Photocatalytic activity

Cationic dye RhB and anionic dye MO were chosen to evaluate the photocatalytic performances of BiOBr-001 and BiOBr-111 under visible light irradiation ($\lambda \geq 420$ nm). As shown in Fig. 5a, it can be clearly seen that BiOBr-111 exhibited higher photocatalytic activity than BiOBr-001. More specifically, RhB dye over BiOBr-111 can be completely degraded in 15 min under visible light irradiation; while over BiOBr-001 needs 45 min. The similar phenomenon can be observed in the degradation of MO. Moreover, the degradation efficiency of RhB is higher than that of MO. Since the as-prepared BiOBr-001 and BiOBr-111 are active under visible light irradiation, indirect dye photosensitization would occur in the experiment. Considering that the adsorption capacity of catalyst is crucial in the dye photosensitization process, the higher catalytic activity for RhB resulted from the enhanced adsorption of cationic dye. It is well-established that {001} facets of BiOX are negatively charged, we can conclude {111} facets are also negatively charged from the above experimental results (Fig. 5a) and atomic structure (Fig. 1e).

In order to further investigate the characteristics of the facets, the adsorption capacities over BiOBr-001 and BiOBr-111 were studied. Fig. 5b shows the adsorption capacities of RhB and MO normalized by special surface area in the dark. The normalized adsorption capacity of RhB over BiOBr-001 is higher than that over BiOBr-111, while the adsorption capacity of MO is quite opposite. The aforementioned structural characteristics reveal that both {111} and {001} facets contain terminal oxygen atoms, but the density of oxygen atoms of {001} facets is higher than that of {111} facets, so {001} facets are expected to be more negatively charged than {111} facets and favorable for the adsorption of positively charged RhB molecules. However, it is difficult for MO to be adsorbed on {001} facets because of the repulsive interaction between negatively charged {001} and anionic dye MO. The open channels of {111} facets offer more active sites and larger accommodation space for the MO adsorption.

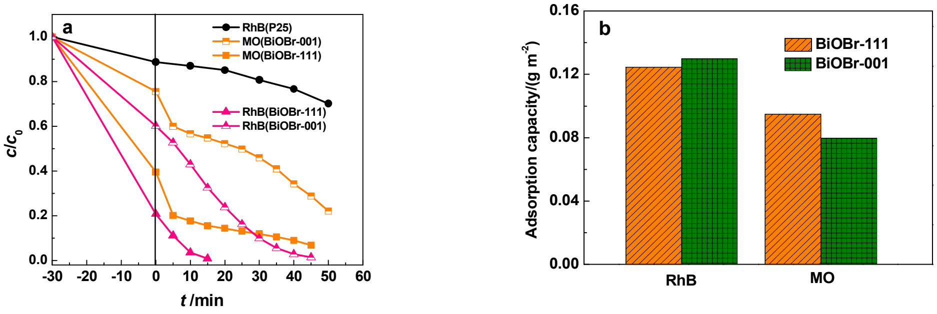

Fig. 5 (a) Photocatalytic degradation efficiencies and (b) normalized adsorption capacities of RhB and MO over BiOBr-001 and BiOBr-111 ($\lambda \geq 420$ nm**).**

To eliminate dye sensitization effect [35], a monochromatic visible light (λ=420 nm) was selected since it has a minimal spectral overlap with RhB. As shown in Fig. 6a, RhB dye over BiOBr-111 can be completely degraded in 80 min under the monochromatic light irradiation; while 63% of RhB is degraded over BiOBr-001. The reaction constant k obtained by plotting $\ln(c_e/c)$ versus irradiation time t was used to evaluate the degradation rate. The k value of BiOBr-111 is 0.032 min^{-1}, much larger than that of BiOBr-001 (0.006 min^{-1}). In addition, the photocatalytic performance of the samples was evaluated by removing gaseous acetone in air under visible light ($\lambda \geq 420$ nm). Fig. 6b shows that BiOBr-111 exhibits higher photocatalytic activity with the acetone removal ratio of 77% in 70 min, superior to BiOBr-001(60%). Therefore, both the above experiments confirm the enhanced photocatalytic performance of BiOBr-111.

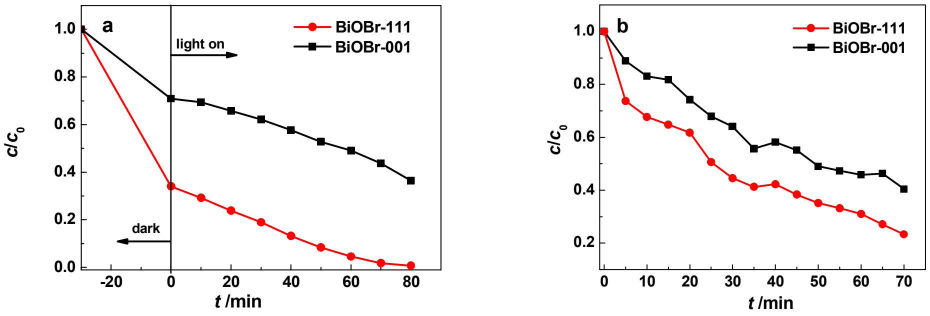

Fig. 6 (a) Photocatalytic degradation efficiencies of RhB under monochromatic visible light (λ**=420 nm) and (b) removal of acetone under visible light irradiation (**$\lambda \geq 420$ **nm).**

It is well known that reducing particle size should affect the band structure of semiconductors, which further affects photocatalytic activity. As shown in UV-vis diffuse reflectance spectroscopy (Fig. 7a), BiOBr-111 exhibits stronger absorption intensity in both the ranges of ultraviolet and visible light than BiOBr-001. This can be ascribed to more spaces between nanosheets in BiOBr-111, which is beneficial to the multi-reflection and scattering of light, and consequently increases effective optical path-length and absorption probability of photons. More importantly, Fig. 7b reveals that the band gap of BiOBr-111 is ~2.56 eV, smaller than that of BiOBr-001(~2.77 eV). Mott-Schottky plots were measured to determine the relative CB positions of the two samples. As shown in Fig. 7c, the flat band potentials of BiOBr-111 and BiOBr-001 were -0.25V and 0.1 V (vs.SCE), respectively. Accordingly, the CB positions of BiOBr-111 and BiOBr-001 are estimated to be -0.49 eV and -0.14 eV(vs. NHE), respectively. Combined with the results of optical measurements, the VB maximum energy of BiOBr-111 occurs at 2.07 eV, and up-shifts by 0.56 eV compared with that of BiOBr-001. The band structures of BiOBr-111 and BiOBr-001 are shown in Fig. 7d. The CB up-shifting of BiOBr-111 not only provides more photo-generated electrons to react with molecular oxygen to generate superoxide ions, but also inhibits electron-hole recombination due to rapid transfer of photoexcited electrons to reactants [36]. On the other hand, the raised VB width of BiOBr-111 promotes the mobility of holes generated, which is beneficial for the photo-oxidation of holes. Therefore, BiOBr-111 exhibits higher photocatalytic activity than BiOBr-001.

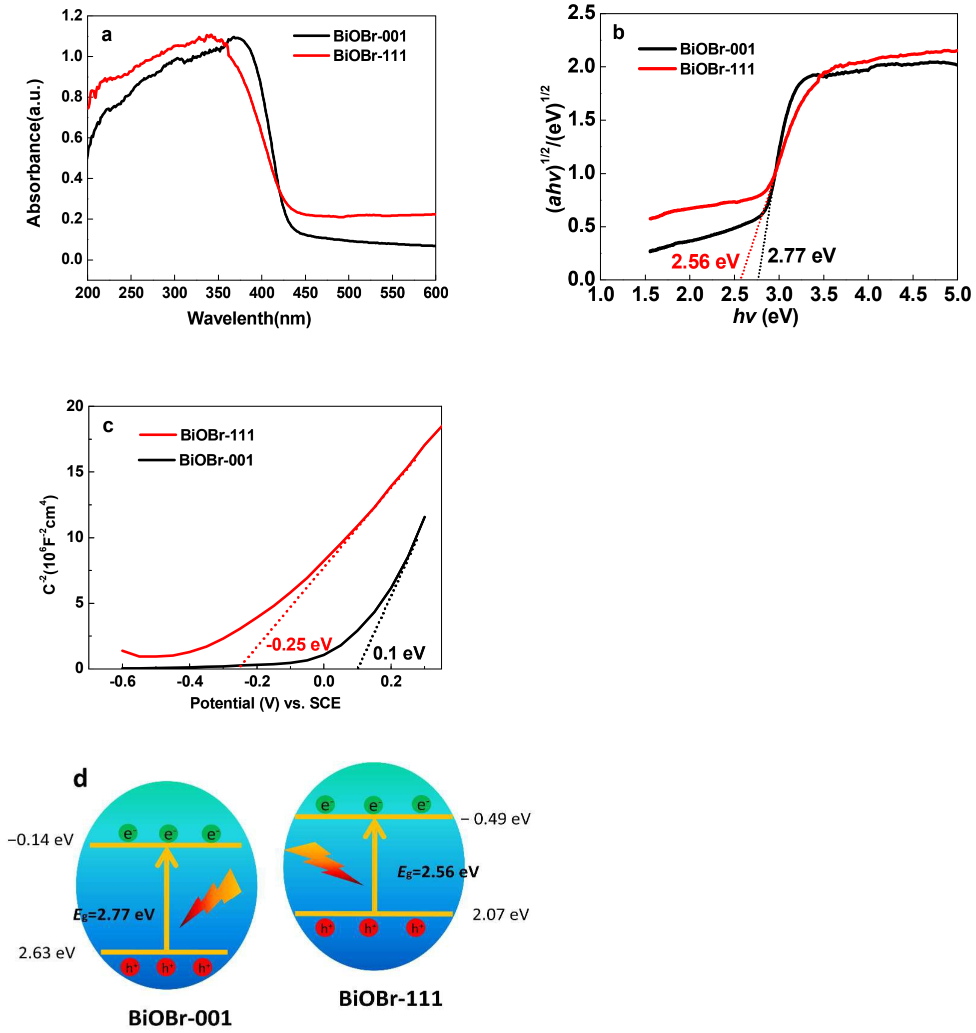

Fig. 7 (a)UV-Vis diffuse reflection spectra, (b) the plots of (*ahv*)$^{1/2}$ vs. photon energy, (c) Mott-Schottky plots and (d) schematic illustration of the band structure of BiOBr-111 and BiOBr-001.

3.7 Photoelectrochemical performance

In order to study the photo-induced charge separation efficiency of the two BiOBr samples, photocurrent transient response under visible light irradiation ($\lambda \geq 420$ nm) and electrochemical impedance spectroscopy (EIS) were carried out. As shown in Fig. 8a, both electrodes generate photocurrent promptly, but the BiOBr-111 film electrode exhibits a higher photocurrent than the BiOBr-001 film electrode, indicating the more efficient photo-induced charge separation and transfer on BiOBr-111. Moreover, the arc radius of BiOBr-111 electrode is clearly smaller than that of BiOBr-001 (Fig. 8b), which further demonstrates that the BiOBr-111 electrode has a higher separation efficiency of photo-generated electron-hole pairs and faster charge-transfer than the BiOBr-001 electrode at the solid-liquid interface. The results of photoelectrochemical test agree well with the above analysis on the band structure of the BiOBr samples.

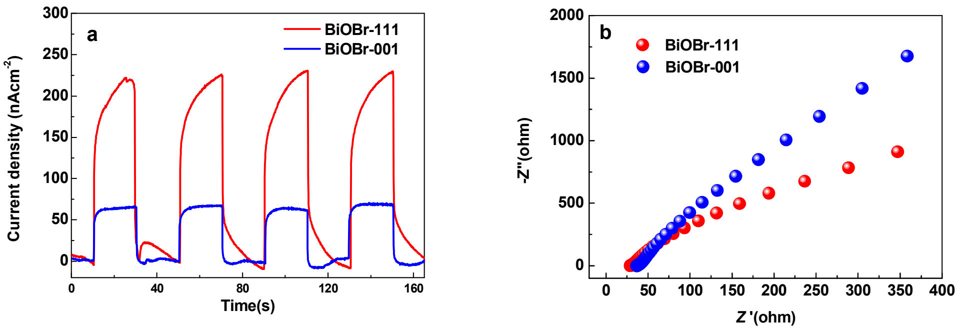

Fig. 8 (a) Photocurrent responses ($\lambda \geq 420$ nm) and (b) Nyquist impedance plots of BiOBr-111 and BiOBr-001 in 0.1 M Na_2SO_4 aqueous solutions

Additionally, to confirm the stability and reusability of BiOBr-111, recycling experiments for the photodegradation of RhB and MO were conducted under visible light irradiation($\lambda \geqslant 420$ nm), as shown in Fig. S2. The photocatalytic efficiencies decrease slightly after three cycles, which can be attributed to the loss of catalyst during recycling and washing process. The results indicate that BiOBr-111 prepared by the facile method is stable for the photodegradation of pollutant molecules, which is important for its practical application.

4. Conclusions

In summary, we have for the first time obtained 3D BiOBr micro-flower partially enclosed by {111} facets with the assistance of anionic surfactant SDS. BiOBr-111 exhibited higher photocatalytic activity for the degradation of dyes and gaseous acetone under visible light irradiation because of higher adsorption capacity and narrower band gap with both up-shifted valence band maximum and conduction band minimum. The findings provide some useful information about {111} facets of BiOX and facet-dependent photocatalytic property.

Acknowledgements

This work was supported by the National Natural Science Foundation of China (21406164，21466035), the National Key Basic Research and Development Program of China (973 program, No. 2014CB239300, and 2012CB720100), Research Fund for the Doctoral Program of Higher Education of China (No. 20110032110037, 20130032120019).

References

[1] Hua Gui Yang, Cheng Hua Sun, Shi Zhang Qiao, Jin Zou, Gang Liu, Sean Campbell Smith, Hui Ming Cheng and Gao Qing Lu, *Nature*, 2008, 453, 638.

[2] Gang Liu, Hua Gui Yang, Xuewen Wang, Lina Cheng, Jian Pan, Gao Qing (Max) Lu and Hui-Ming Cheng, *J. Am. Chem. Soc.*, 2009, 131, 12868.

[3] Hua Gui Yang, Gang Liu, Shi Zhang Qiao, Cheng Hua Sun,Yong Gang Jin, Sean Campbell Smith, Jin Zou, Hui Ming Cheng and Gao Qing (Max) Lu, *J. Am. Chem. Soc.*, 2009, 131, 4078.

[4] Liang Sun, Ying Qin, Qingqing Cao, Bingqing Hu, Zhiwei Huang, Ling Ye and Xingfu Tang, *Chem. Commun.*, 2011, 47, 12628.

[5] Yuka Aoyama, Yuya Oaki, Ryuta Ise and Hiroaki Imai, *CrystEngComm*, 2012, 14, 1405.

[6] Haimin Zhang, Xiaolu Liu,Yun Wang, Porun Liu,Weiping Cai, Guangshan Zhu,Huagui Yang and Huijun Zhao, *J. Mater. Chem. A*, 2013, 1, 2646.

[7] Jiaguo Yu, Jingxiang Low, Wei Xiao, Peng Zhou and Mietek Jaroniec, *J. Am. Chem. Soc.*, 2014, 136, 8839.

[8] Rengui Li, Hongxian Han, Fuxiang Zhang, Donge Wang and Can Li, *Energy Environ. Sci.*, 2014, 7, 1369.

[9] Kyoung E. Kweon and Gyeong S. Hwang, *Appl. Phys. Lett.*, 2013, 103, 131603.

[10] Yingpu Bi, Shuxin Ouyang, Naoto Umezawa, Junyu Cao and Jinhua Ye, *J. Am. Chem. Soc.*, 2011, 133, 6490.

[11] Hongyan Hu, Zhengbo Jiao, Hongchao Yu, Gongxuan Lu, Jinhua Ye and Yingpu Bi, *J. Mater. Chem. A*, 2013, 1, 2387.

[12] David James Martin, Naoto Umezawa, Xiaowei Chen, Jinhua Ye and Junwang Tang, *Energy Environ. Sci.*, 2013, 6, 3380.

[13] Zhengbo Jiao, Yan Zhang, Hongchao Yu, Gongxuan Lu, Jinhua Ye and Yingpu Bi, *Chem. Commun.*, 2013, 49, 636.

[14] Zhaoke Zheng, Baibiao Huang, Zeyan Wang, Meng Guo, Xiaoyan Qin, Xiaoyang Zhang, Peng Wang and Ying Dai, *J. Phys. Chem. C*, 2009, 113, 14448.

[15] Gang Liu, Hua Gui Yang, Jian Pan, Yong Qiang Yang, Gao Qing (Max) Lu and Hui-Ming Cheng, *Chem. Rev.*, 2014, 114, 9559.

[16] Hefeng Cheng, Baibiao Huang and Ying Dai, *Nanoscale*, 2014, 6, 2009.

[17] Ye Tian, Chuan Fei Guo, Yanjun Guo, Qi Wang and Qian Liu, *Applied Surface Science*, 2012,258, 1949.

[18] Jinyan Xiong, Gang Cheng, Guangfang Li, Fan Qin and Rong Chen, *RSC Advances*, 2011, 1, 1542.

[19] Chonghai Deng and HanminGuan, *Materials Letters*, 2013, 107,119.

[20] Gang Cheng,Jinyan Xiong and Florian J. Stadler, *New J.Chem.,* 2013, **37**, 3207.

[21] Kun Zhang, Jie Liang, Shan Wang,Jie Liu,Kuaixia Ren,Xiao Zheng, Hui Luo,Yingjie Peng, Xing Zou,Xu Bo, Jihong Li and Xibin Yu, *Cryst. Growth Des*., 2012,12, 793.

[22] Bin Zhang, Guangbin Ji, Yousong Liu, M.A. Gondal, Xiaofeng ChangBin Zhang, Guangbin Ji, Yousong Liu, M.A. Gondal and Xiaofeng Chang, *Catalysis Communications*, 2013, 36, 25.

[23] Guohua Jiang, Xiaohong Wang, Zhen Wei,Xia Li, Xiaoguang Xi, Ruanbing Hu, Bolin Tang, Rijing Wang, Sheng Wang, Tao Wang and Wenxing Chen, *J. Mater. Chem. A*, 2013, 1, 2406.

[24] Jie Fu, Yanlong Tian, Binbin Chang, Fengna Xi and Xiaoping Dong, *J. Mater. Chem.*, 2012, 22, 21159.

[25] Tian Bao Li, Gang Chen,Chao Zhou, Zao Yu Shen, Ren Cheng Jin and Jing Xue Sun, *Dalton Trans.*, 2011, 40, 6751.

[26] Liqun Ye, Ling Zan, Lihong Tian, Tianyou Peng and Jiujun Zhang, *Chem. Commun.*, 2011, 47, 6951.

[27] Jing Jiang, Kun Zhao, Xiaoyi Xiao and Lizhi Zhang, *J. Am. Chem. Soc.*, 2012, 134, 4473.

[28] Dong-Hong Wang, Gui-Qi Gao,Yue-Wei Zhang, Li-Sha Zhou, An-Wu Xu and Wei Chen, *Nanoscale*, 2012, 4, 7780.

[29] Anupam Biswas, Raja Das, Chandan Dey, Rahul Banerjee and Pankaj Poddar, *Cryst. Growth Des.*, 2014, 14, 236.

[30] Da Zhang, Jing Li, Qigang Wang and Qingsheng Wu, *J. Mater. Chem. A*, 2013, 1, 8622.

[31] Jing Chen, Meili Guan, Weizheng Cai, Jinju Guo,Chong Xiao and Gaoke Zhang, *Phys.Chem.Chem.Phys*., 2014, 16, 20909.

[32] Haijun Zhang, Yuxiao Yang, Zhen Zhou, Yaping Zhao and Lu Liu, *J. Phys. Chem. C*, 2014, 118, 14662.

[33] Jie Li, Ying Yu and Lizhi Zhang, *Nanoscale*, 2014, 6, 8473.

[34] K. K. Banger, Y. Yamashita, K. Mori, R. L. Peterson, T. Leedham, J. Rickard and H. Sirringhaus, *Nat Mater*, 2011, 10, 45.

[35] Sugyeong Baea, Sujeong Kim, Seockheon Lee and Wonyong Choi, *Catalysis Today*, 2014, 224, 21.

[36] Gang Liu, Ping Niu, Chenghua Sun, Sean C. Smith, Zhigang Chen, Gao Qing (Max) Lu and Hui-Ming Cheng, *J. Am. Chem. Soc.*, 2010, 132, 11642.

Electronic supplementary information (ESI) available: SEM images in time-dependent experiment, and cycling degradation test.

.